Supplementary Information for

Emerging Two-dimensional Group IV Chalcogenides as Building Blocks for Advanced Infrared Photodetector

Hao Chen[1], Sijie Shen[1], Rui Xiong[2,*], Huiwen Yu[1], Jiansen Wen[1], Xiaochun Huang[3,*], Cuilian Wen[1], Bo Wu[1], Baisheng Sa[1,*]

[1]*Multiscale Computational Materials Facility, State Key Laboratory of Green and Efficient Development of Phosphorus Resources, College of Materials Science and Engineering, Fuzhou University, Fuzhou 350108, China.*
[2]*State Key Laboratory of Photocatalysis on Energy and Environment, College of Chemistry, Fuzhou University, Fuzhou 350108, China.*
[3]*Physikalisches Institut, Experimentelle Physik II, Universität Würzburg, Am Hubland, 97074 Würzburg, Germany.*

Corresponding Author: 398523@fzu.edu.cn (R. Xiong); xiaochun.huang@uni-wuerzburg.de (X. Huang); bssa@fzu.edu.cn (B. Sa)

Table S1 The formation energy E_{form} was calculated using the total energy (eV) of the 2D monolayer and the reference energies of the constituent elements in their stable bulk phases. For the bulk phase calculations, a *k*-point mesh of 12 × 12 × 12 was employed with the PREC = Accurate setting in VASP, while all other parameters remained at their default values.

System	Total energy
Te-Si-Si-Te	-17.580
Te-Si-Ge-Te	-16.856
Te-Si-Sn-Te	-16.402
Te-Si-Pb-Te	-15.921
Te-Si-Si-Se	-18.313
Te-Si-Ge-Se	-17.518
Te-Si-Sn-Se	-17.110
Te-Si-Pb-Se	-16.587
Si	-5.571
Ge	-4.684
Sn	-4.025
Pb	-3.792
Se	-3.367
Te	-3.648

Table S2 The effective mass m^*, deformation potentials E_1 (eV), elastic moduli C_{2D} (N/m) and carrier mobility μ ($cm^2V^{-1}s^{-1}$) of the 2D X-A-A'-X'.

System	Direction	Carrier type	E_1	C_{2D}	m^*/m_0	μ
Te-Si-Si-Te	x	e	6.403	51.378	0.110	807.568
		h	4.487	51.378	0.222	283.546
	y	e	6.508	50.109	0.825	101.654
		h	3.990	50.109	3.371	23.031
Te-Si-Ge-Te	x	e	5.978	5.676	0.342	60.052
		h	4.672	5.676	0.212	68.509
	y	e	5.926	23.643	0.080	1088.254
		h	3.900	23.643	0.688	126.196
Te-Si-Sn-Te	x	e	5.923	5.725	0.147	227.753
		h	4.596	5.725	0.284	88.917
	y	e	5.960	29.418	0.073	2327.515
		h	3.958	29.418	0.184	950.903
Te-Si-Pb-Te	x	e	6.130	9.582	2.302	2.618
		h	4.764	9.582	0.320	36.561
	y	e	6.061	11.361	0.354	20.642
		h	3.583	11.361	1.853	13.233
Te-Si-Si-Se	x	e	6.353	52.104	1.931	33.643
		h	4.435	52.104	0.113	5103.999
	y	e	6.311	72.186	0.093	980.701
		h	3.794	72.186	0.085	12845.231
Te-Si-Ge-Se	x	e	6.467	32.304	4.120	2.163
		h	4.960	32.304	0.249	361.788
	y	e	6.490	53.056	0.830	17.513
		h	4.287	53.056	0.388	510.461
Te-Si-Sn-Se	x	e	6.456	26.005	1.460	26.353
		h	5.095	26.005	0.399	108.223
	y	e	6.470	11.994	0.082	215.465
		h	4.558	11.994	0.615	40.462
Te-Si-Pb-Se	x	e	6.758	22.424	1.301	24.109
		h	5.598	22.424	0.506	29.933
	y	e	6.736	7.832	0.086	128.226
		h	5.062	7.832	2.009	3.221

Table S3 Summary of key optical absorption metrics for the 2D X-A-A'-X'. Listed are the maximum absorption coefficient from the infrared to visible range, J_{max} (cm^{-1}), and its corresponding photon energy E_p (eV), together with the maximum absorption coefficient in the infrared region, *J*IR max (cm^{-1}), and its corresponding photon energy *E*IR P (eV).

System	E_p	J_{max}	*E*IR P	*J*IR max
Te-Si-Si-Te	3.15	7.44×10^5	0.75	2.50×10^5
Te-Si-Ge-Te	3.07	6.96×10^5	1.43	2.41×10^5
Te-Si-Sn-Te	2.27	5.65×10^5	1.47	2.41×10^5
Te-Si-Pb-Te	2.83	5.10×10^5	1.63	2.06×10^5
Te-Si-Si-Se	2.40	6.89×10^5	1.40	2.69×10^5
Te-Si-Ge-Se	2.93	5.65×10^5	1.63	2.55×10^5
Te-Si-Sn-Se	2.60	6.04×10^5	1.63	2.26×10^5
Te-Si-Pb-Se	3.13	5.60×10^5	1.50	1.33×10^5

Table S4 A comparative analysis of maximum photocurrent density *J*max ph (A/m^2): this work versus prior studies with identical computational frameworks.

Material	*J*max ph	Ref
InGeSe monolayer	19.4	S1
$Hg_{0.75}Cd_{0.25}Te$	12.3	S2
$MoSi_2N_4$ monolayer	14.79	S3
MoSePCl monolayer	33.3	S4
$VSiN_3$ homojunction	21.43	S5
InSe homojunction	32.10	S6
WSSe/g-GeC heterojunction	~4	S7
MoSSe/Te heterojunction	32	S8
In_2Se_3/MoS_2 heterojunction	-5	S9
GeC/SSnSe heterojunction	10.43	S10
Te-Si-Pb-Te/Sb_2Te_3 heterojunction	36.33	This work
Te-Si-Si-Se/Sb_2Te_3 heterojunction	114.61	This work
Te-Si-Ge-Se/Sb_2Te_3 heterojunction	23.85	This work

Table S5 A comparative analysis of maximum photoresponsivity *R*max ph (A/W) in the infrared region: this work versus prior experimental studies.

Material	*R*max ph	Ref
BP	4.8×10^{-3}	S11
MoS_2	0.57	S12
ZnO/ZnTe	0.196	S13
MoS_2/GaAs	0.527	S14
MoS_2/Si	0.3	S15
WSe_2/MoS_2	0.32	S16
MoS_2/graphene/WSe_2	0.1	S17
PbSe/TiO_2/Gr	0.506	S18
Te-Si-Pb-Te/Sb_2Te_3 heterojunction	1.51	This work
Te-Si-Si-Se/Sb_2Te_3 heterojunction	5.31	This work
Te-Si-Ge-Se/Sb_2Te_3 heterojunction	1.11	This work

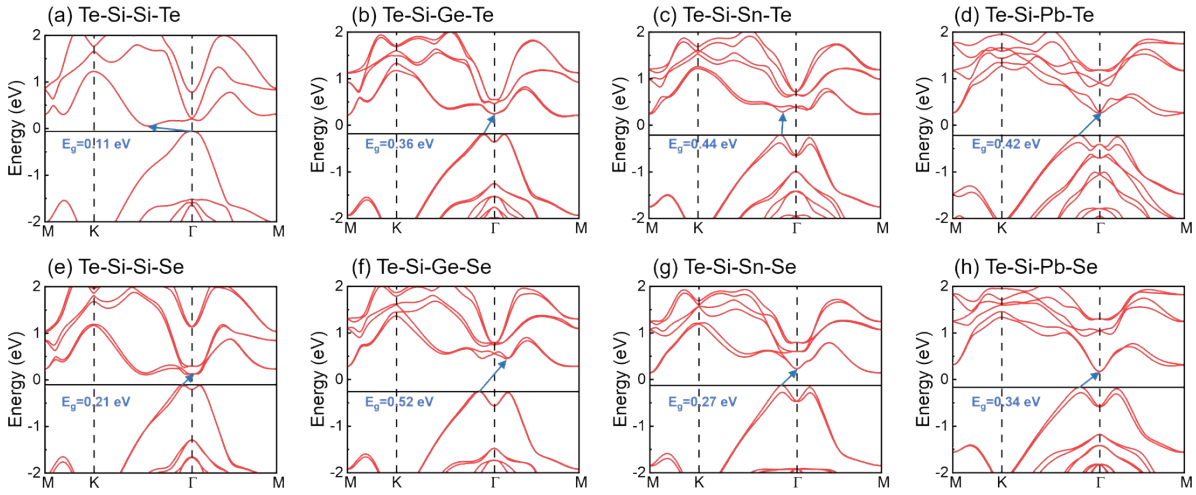

Fig. S1 Electronic structures for 2D X-A-A'-X' monolayers. The calculated band structures of **(a)** Te-Si-Si-Te, **(b)** Te-Si-Ge-Te, **(c)** Te-Si-Sn-Te, **(d)** Te-Si-Pb-Te, **(e)** Te-Si-Si-Se, **(f)** Te-Si-Ge-Se, **(g)** Te-Si-Sn-Se, **(h)** Te-Si-Pb-Se using PBE with SOC. The Fermi level is set to VBM.

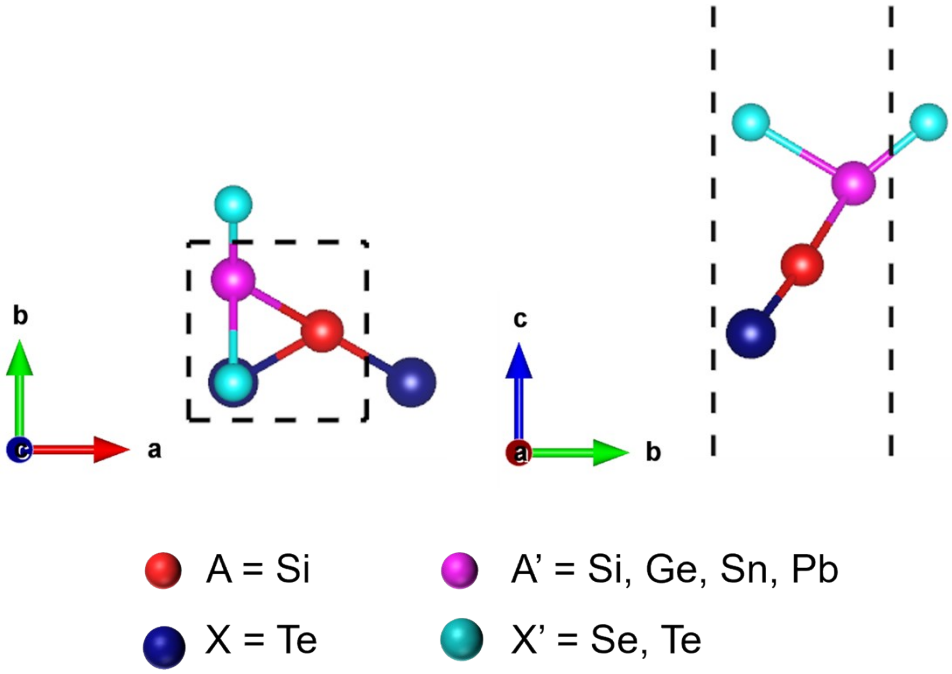

Fig. S2 The orthorhombic structure sketch of 2D X-A-A'-X'. An orthorhombic lattice instead of the traditional hexagonal lattice was adopted to calculate the intrinsic responses to uniaxial strain in the 2D X-A-A'-X'.

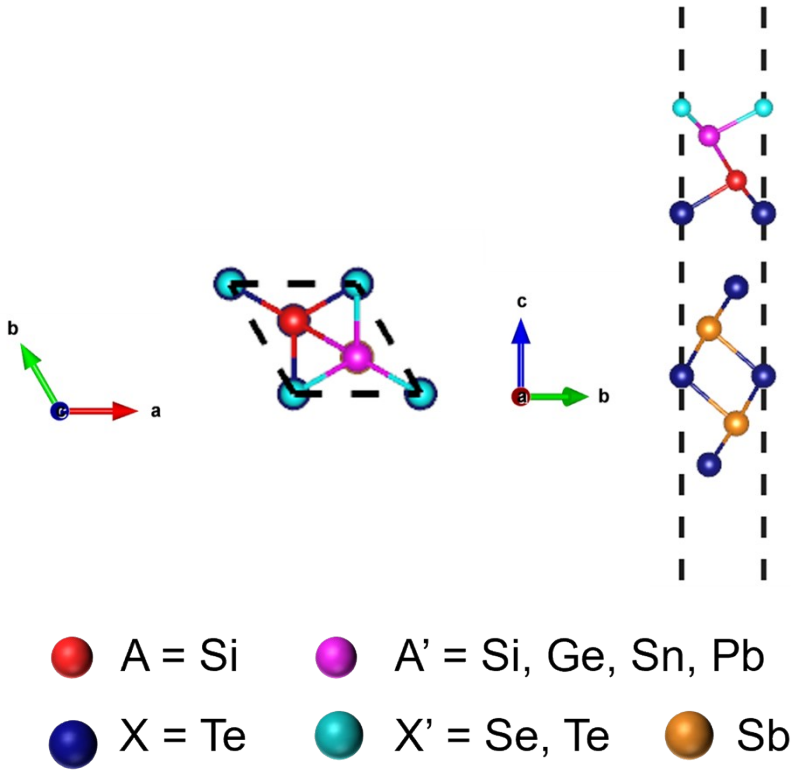

Fig. S3 The structure sketch of 2D X-A-A'-X'/Sb_2Te_3 vdW heterostructures.

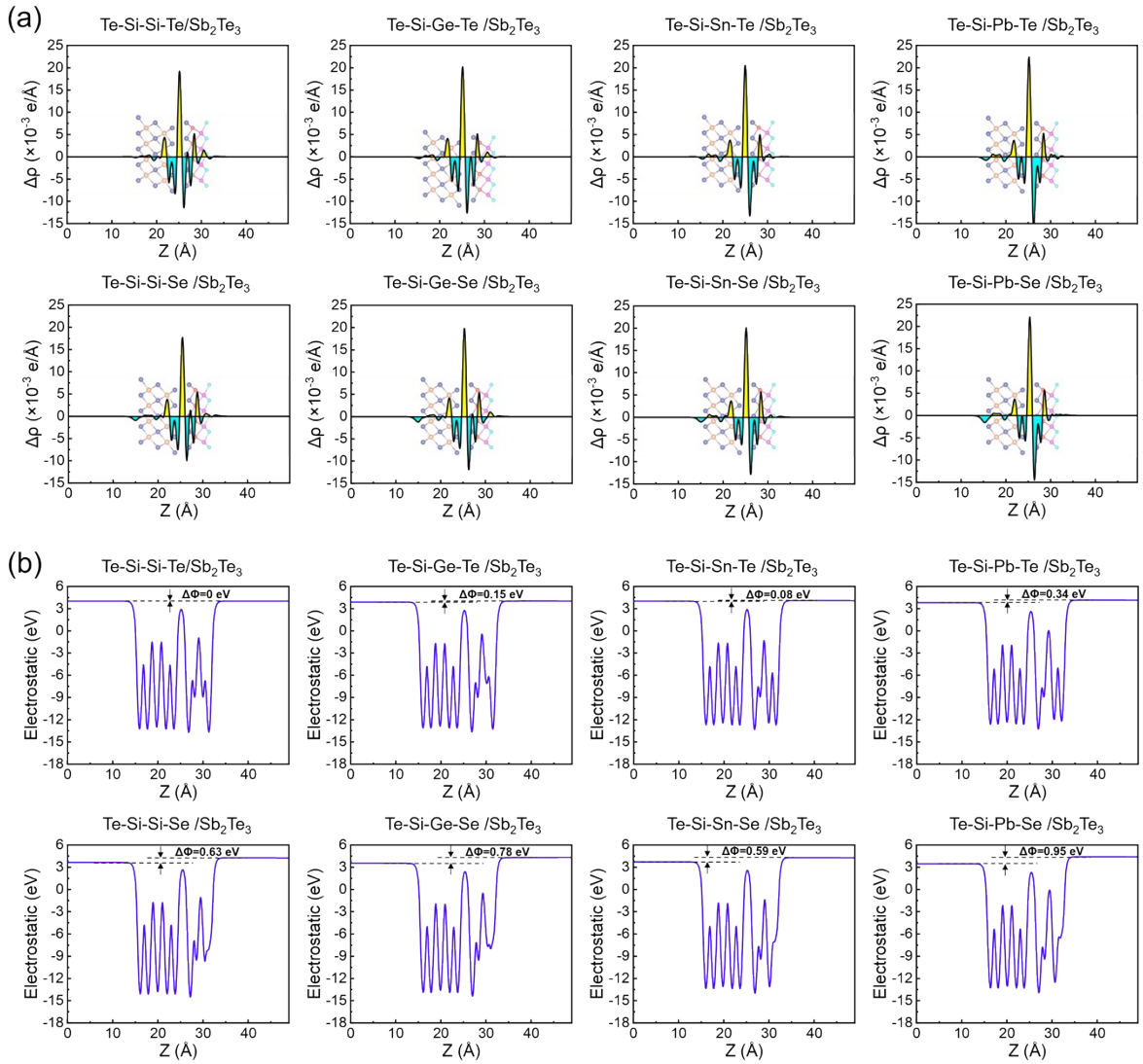

Fig. S4 Charge transfer. Planar-averaged (a) charge density difference and electrostatic potential of X-A-A'-X'/Sb_2Te_3 heterostructure along the Z direction.

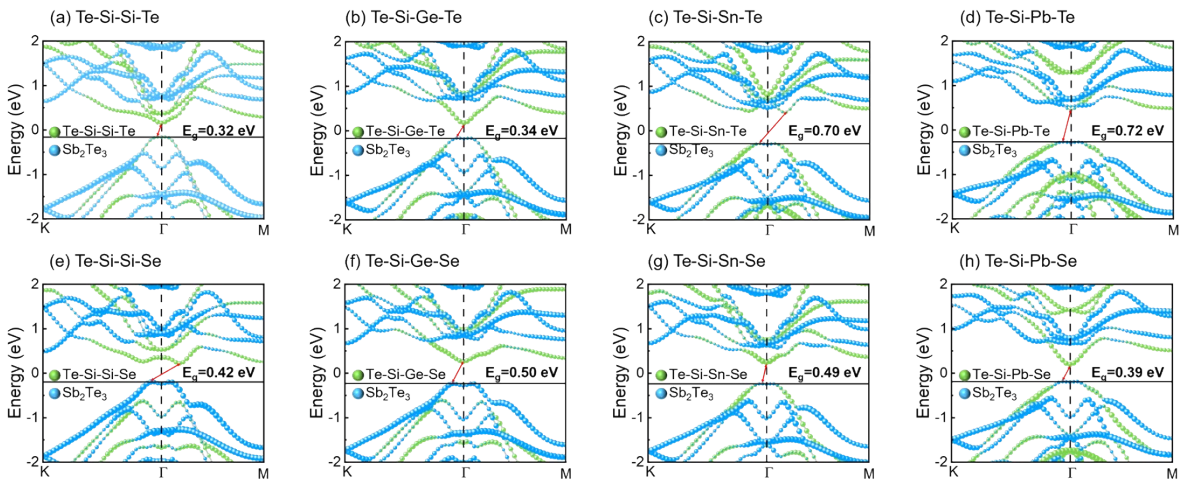

Fig. S5 Electronic structures for X-A-A'-X'/ Sb_2Te_3 vdW heterostructures. The calculated band structures of **(a)** Te-Si-Si-Te/Sb_2Te_3, **(b)** Te-Si-Ge-Te/Sb_2Te_3, **(c)** Te-Si-Sn-Te/Sb_2Te_3, **(d)** Te-Si-Pb-Te/Sb_2Te_3, **(e)** Te-Si-Si-Se/Sb_2Te_3, **(f)** Te-Si-Ge-Se/Sb_2Te_3, **(g)** Te-Si-Sn-Se/Sb_2Te_3 and **(h)** Te-Si-Pb-Se/Sb_2Te_3 vdW heterostructures using HSE06. The green spheres represent 2D X-A-A'-X', and blue spheres represent Sb_2Te_3 monolayer

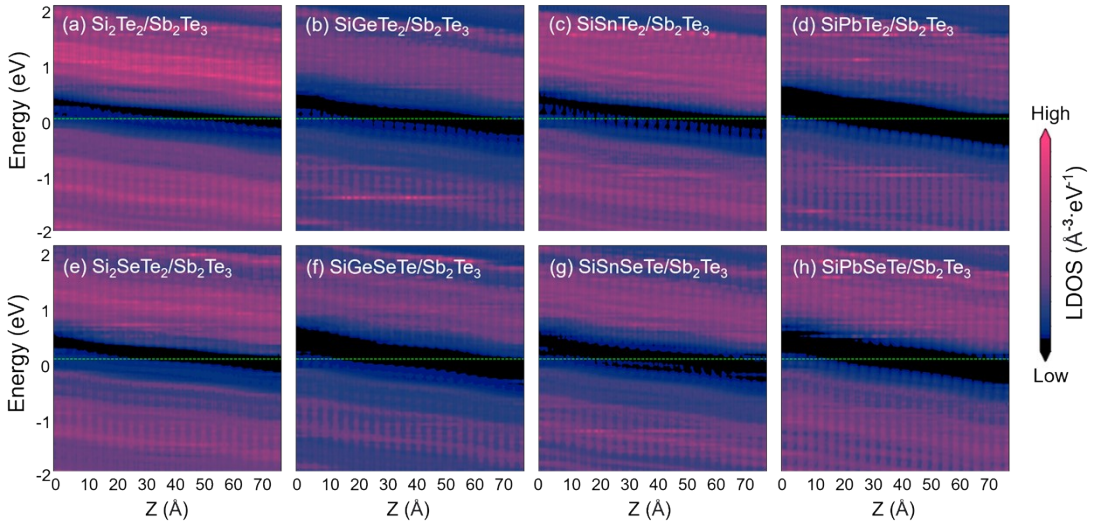

Fig. S6 Projected local density of states. The projected local density of states of **(a)** Te-Si-Si-Te/Sb_2Te_3, **(b)** Te-Si-Ge-Te/Sb_2Te_3, **(c)** Te-Si-Sn-Te/Sb_2Te_3, **(d)** Te-Si-Pb-Te/Sb_2Te_3, **(e)** Te-Si-Si-Se/Sb_2Te_3, **(f)** Te-Si-Ge-Se/Sb_2Te_3, **(g)** Te-Si-Sn-Se/Sb_2Te_3 and **(h)** Te-Si-Pb-Se/Sb_2Te_3-based p-i-n junctions. The horizontal coordinate is the *z*-direction and the green dashed line represents the Fermi level.

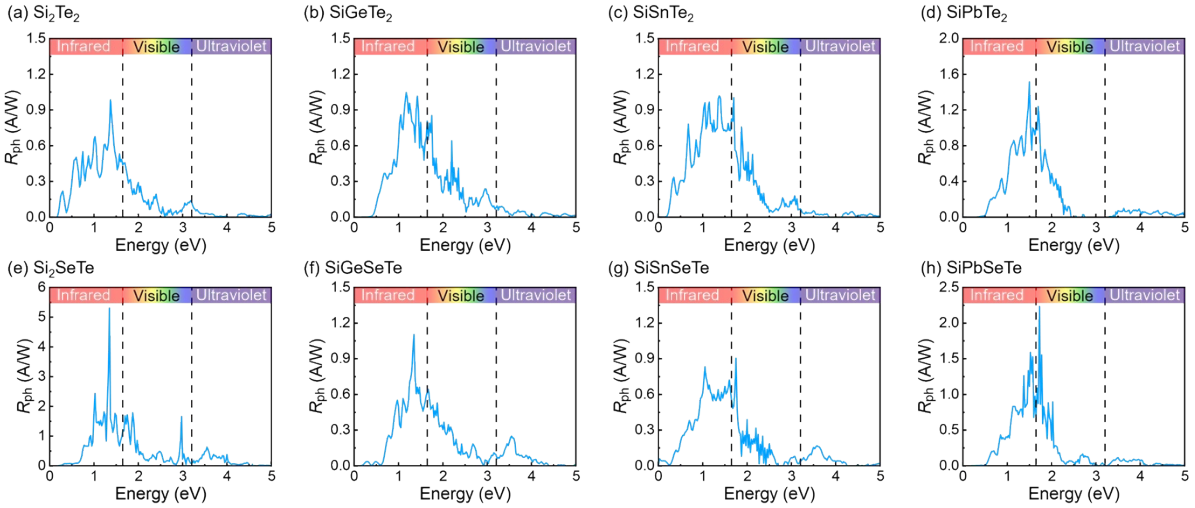

Fig. S7 Photoresponsivity. Photoresponsivity as a function of photon energy for **(a)** Te-Si-Si-Te/Sb_2Te_3, **(b)** Te-Si-Ge-Te/Sb_2Te_3, **(c)** Te-Si-Sn-Te/Sb_2Te_3, **(d)** Te-Si-Pb-Te/Sb_2Te_3, **(e)** Te-Si-Si-Se/Sb_2Te_3, **(f)** Te-Si-Ge-Se/Sb_2Te_3, **(g)** Te-Si-Sn-Se/Sb_2Te_3 and **(h)** Te-Si-Pb-Se/Sb_2Te_3-based p-i-n junctions.

References

S1. R. Xiong, F. Zeng, Z. Cui, C. Wen, B. Sa and C. Yang, *Phys. Chem. Lett.*, 2025, **16**, 9070-9077.

S2. R. Mamindla, S. Chakraborty and M. K. Niranjan, *J. Appl. Phys.*, 2025, **138**, 113103.

S3. P. Guo, L. Li, M. Li and J. Wang, *Solid State Commun.*, 2025, **406**, 116204.

S4. S. Soleimani-Amiri, S. Gholami Rudi and N. Ghobadi, *Nanoscale*, 2025, **17**, 16748-16766.

S5. Z. Cui, C. Huang, Y. Yu, R. Xiong, C. Wen and B. Sa, *Surf. Interfaces*, 2024, **54**, 105160.

S6. L. Li, P. Yuan, T. Liu, Z. Ma, C. Xia and X. Li, *Phys. Rev. Appl*, 2023, **19**, 014039.

S7. Y. Yu, G. Liu, C. Luo, W. Yang, X. Xiao and T. Chen, *ACS Appl. Nano Mater.*, 2024, **7**, 18299-18308.

S8. B. Zhou, A. Cui, L. Gao, K. Jiang, L. Shang, J. Zhang, Y. Li, S.-J. Gong, Z. Hu and J. Chu, *Phys. Rev. Mater*, 2021, **5**, 125404.

S9. B. Zhou, K. Jiang, L. Shang, J. Zhang, Y. Li, L. Zhu, S.-J. Gong, Z. Hu and J. Chu, *J. Mater. Chem. C*, 2020, **8**, 11160-11167.

S10. X. Jiang, W. Xie, X. Xu, Q. Gao, D. Li, B. Cui, D. Liu and F. Qu, *Nanoscale*, 2022, **14**, 7292-7302.

S11. M. Buscema, D. J. Groenendijk, S. I. Blanter, G. A. Steele, H. S. J. van der Zant and A. Castellanos-Gomez, *Nano Lett.*, 2014, **14**, 3347-3352.

S12. D.-S. Tsai, K.-K. Liu, D.-H. Lien, M.-L. Tsai, C.-F. Kang, C.-A. Lin, L.-J. Li and J.-H. He, *ACS Nano*, 2013, **7**, 3905-3911.

S13. D. You, C. Xu, W. Zhang, J. Zhao, F. Qin and Z. Shi, *Nano Energy*, 2019, **62**, 310-318.

S14. C. Jia, D. Wu, E. Wu, J. Guo, Z. Zhao, Z. Shi, T. Xu, X. Huang, Y. Tian and X. Li, *J. Mater. Chem. C*, 2019, **7**, 3817-3821.

S15. L. Wang, J. Jie, Z. Shao, Q. Zhang, X. Zhang, Y. Wang, Z. Sun and S.-T. Lee, *Adv. Funct. Mater.*, 2015, **25**, 2910-2919.

S16. Q. Wu, L. Li, C. Wang, Z. Wang, Z. Weng, Y. Jiang, L. Lin, X. Gu, E. C. Angel, A. E. Sachat, P. Xiao, H. Nan and S. Xiao, *Adv. Opt. Mater.*, 2025, **13**, 2402378.

S17. M. Long, E. Liu, P. Wang, A. Gao, H. Xia, W. Luo, B. Wang, J. Zeng, Y. Fu, K. Xu, W. Zhou, Y. Lv, S. Yao, M. Lu, Y. Chen, Z. Ni, Y. You, X. Zhang, S. Qin, Y. Shi, W. Hu, D. Xing and F. Miao, *Nano Lett.*, 2016, **16**, 2254-2259.

S18. K. K. Manga, J. Wang, M. Lin, J. Zhang, M. Nesladek, V. Nalla, W. Ji and K. P. Loh, *Adv. Mater.*, 2012, **24**, 1697-1702.